Downloaded from rsta.royalsocietypublishing.org

PHILOSOPHICAL TRANSACTIONS OF THE ROYAL SOCIETY A MATHEMATICAL, PHYSICAL & ENGINEERING SCIENCES

Direct Determination of Interface Structure and Bonding with the Scanning Transmission Electron Microscope

S. J. Pennycook, N. D. Browning, M. M. McGibbon, A. J. McGibbon, D. E. Jesson and M. F. Chisholm

Phil. Trans. R. Soc. Lond. A 1996 **354**, 2619-2634
doi: 10.1098/rsta.1996.0119

Email alerting service

Receive free email alerts when new articles cite this article - sign up in the box at the top right-hand corner of the article or click **here**

To subscribe to *Phil. Trans. R. Soc. Lond. A* go to:
http://rsta.royalsocietypublishing.org/subscriptions

This journal is © 1996 The Royal Society

Downloaded from rsta.royalsocietypublishing.org

Direct determination of interface structure and bonding with the scanning transmission electron microscope

By S. J. Pennycook[1], N. D. Browning[2], M. M. McGibbon[3], A. J. McGibbon[3], D. E. Jesson[1] and M. F. Chisholm[1]

[1]*Solid State Division, Oak Ridge National Laboratory, Oak Ridge, TN 37831–6030, USA*

[2]*Department of Physics (M/C 273), University of Illinois at Chicago, 845 West Taylor Street, Chicago, IL 60607–7059, USA*

[3]*Department of Physics and Astronomy, University of Glasgow, Glasgow G12 8QQ, UK*

The scanning transmission electron microscope is capable of forming an electron probe of atomic dimensions, allowing incoherent imaging and microanalysis to be achieved at atomic resolution. Images formed using elastically scattered electrons show strong atomic number (Z) contrast and reveal atomic column locations without the need for preconceived structure models. Column positions and scattering power can be directly retrieved by a maximum entropy analysis. The Z-contrast image also allows the probe to be positioned with atomic precision over selected atomic columns or planes, making possible atomic-resolution electron energy loss spectroscopy. Interfacial structure and bonding can both be determined directly from experimental data, often leading to unexpected insights. In $SrTiO_3$, grain boundary structural units were identified, and found to be reconstructed, an efficient way to overcome the problem of like-ion repulsion in ionic materials. At a CdTe–GaAs [001] interface, 60° dislocations were directly identified to be of glide type, while in the case of Lomer dislocations, an unexpected core structure was found comprising a four-fold ring structure. With these techniques, dislocation core structure and impurity segregation may be studied experimentally at the atomic scale.

1. Atomic-resolution incoherent imaging and spectroscopy

With a scanning transmission electron microscope (STEM) capable of forming a probe of atomic dimensions, a new approach to interface structure determination becomes possible. Incoherent imaging conditions can be established simultaneously for elastically and inelastically scattered electrons, which enables the direct determination of interfacial structure and bonding from experimental data. This avoids the reliance on preconceived atomic models that is necessary with other structure determination methods such as X-ray diffraction or high-resolution phase contrast microscopy. Incoherent imaging is based on intensities not phases, and so a direct structure inversion becomes possible. With the advent of the 300 kV STEM, the resolution today is sufficient to both resolve and distinguish the sublattice in compound

Phil. Trans. R. Soc. Lond. A (1996) **354**, 2619–2634
Printed in Great Britain

© 1996 The Royal Society
TEX Paper

The Royal Society is collaborating with JSTOR to digitize, preserve, and extend access to *Philosophical Transactions: Mathematical, Physical and Engineering Sciences.* www.jstor.org

Downloaded from rsta.royalsocietypublishing.org

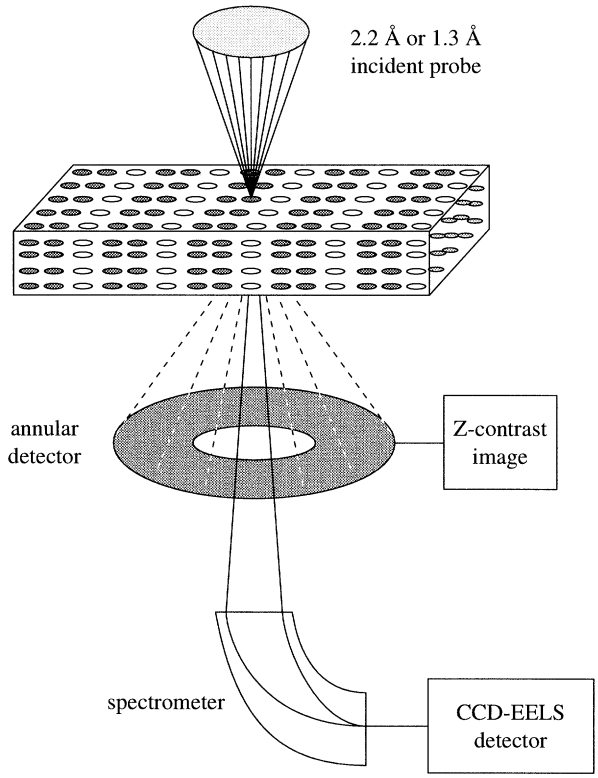

Figure 1. Schematic showing the optical arrangement for atomic imaging and analysis with the scanning transmission electron microscope.

semiconductors, allowing core structures of dislocations to be investigated directly for the first time. In conjunction with electron energy loss spectroscopy (EELS), complementary information on local bonding can be obtained, also with atomic resolution.

The optical arrangement of the STEM differs significantly from its conventional counterpart (Crewe 1980). As seen in figure 1, the objective lens, the critical element in the optical system, is placed before the specimen and used to form a small probe which is scanned across the specimen. Images are formed by detecting a suitable signal as the probe scans, in serial form. If an annular detector is used to collect elastically scattered electrons, the resulting images have a very different character from the phase contrast images of conventional high-resolution microscopes (Crewe *et al.* 1970; Crewe & Wall 1970; Engel *et al.* 1974). The annular detector collects electrons scattered over a wide range of angles, which averages over the phase relationships between diffracted beams leading to an *incoherent* image (Pennycook & Jesson 1990, 1991, 1992; Jesson & Pennycook 1993, 1995; Pennycook *et al.* 1993). The image is given by a convolution of the probe intensity profile with an appropriate object function centred on the atomic columns. Images of atomic columns do not reverse contrast with specimen thickness or objective lens focus as do conventional phase contrast images, so that the positions of atomic columns may be read directly from the image to a high degree of precision without any prior knowledge. The simulated images in figure 2 show the expected appearance of silicon viewed along the [110] axis for a range of defocus values, with parameters chosen appropriate to the VG Micro-

Downloaded from rsta.royalsocietypublishing.org

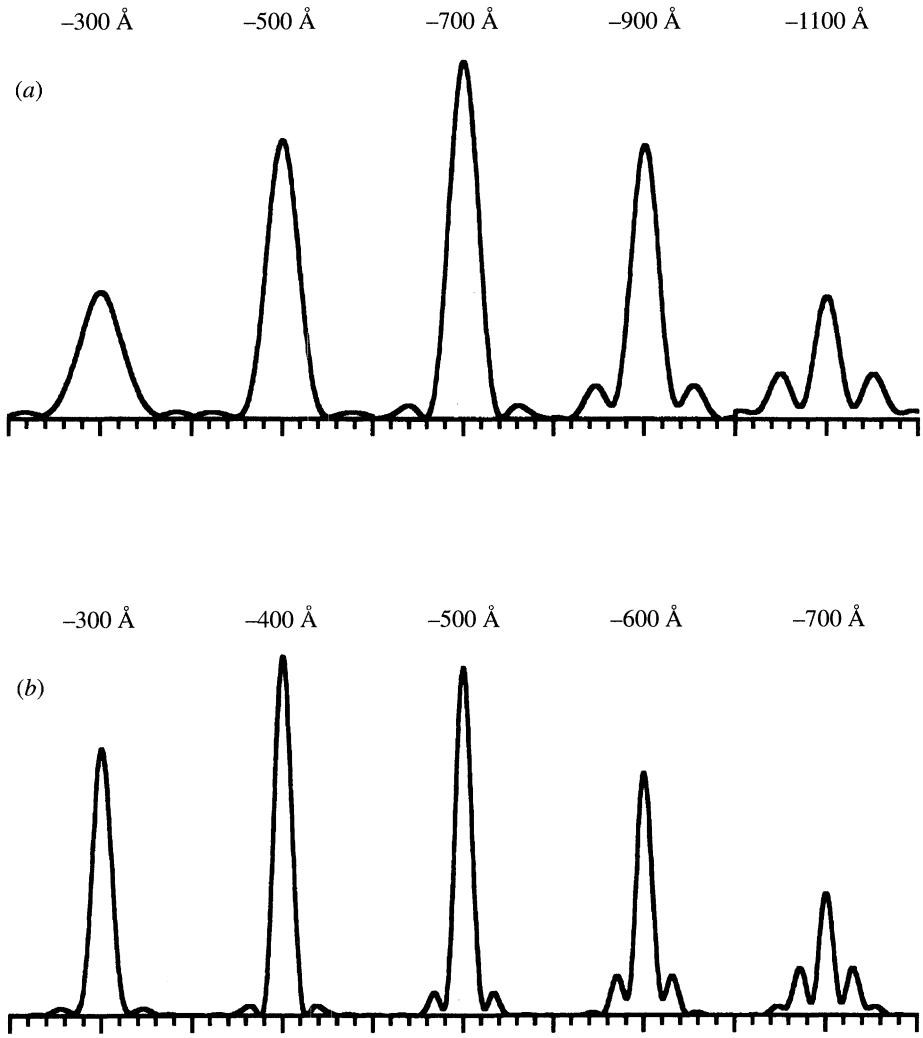

Figure 2. Simulated through focal series for Si⟨110⟩ with corresponding probe intensity profiles for: (*a*) the 100 kV STEM (probe size 2.2 Å); (*b*) the 300 kV STEM (probe size 1.3 Å), predicting resolution of the column pairs or 'dumbbells'.

scopes HB501UX (100 kV) and HB603U (300 kV) installed at Oak Ridge National Laboratory. The optimum focus is that which gives maximum image contrast, when the bright regions of the image correspond accurately with the atomic columns. At 100 kV, with a probe size of 2.2 Å, the closely spaced pairs of columns (dumbbells) are unresolved, but at 300 kV, with a 1.3 Å probe, they are resolved. Columns of different atomic number (Z) are seen with a brightness dependent on their scattering power, roughly proportional to Z^2. The key advantage of incoherent imaging is the direct and intuitive correspondence between object and image. As no simulations are

Downloaded from rsta.royalsocietypublishing.org

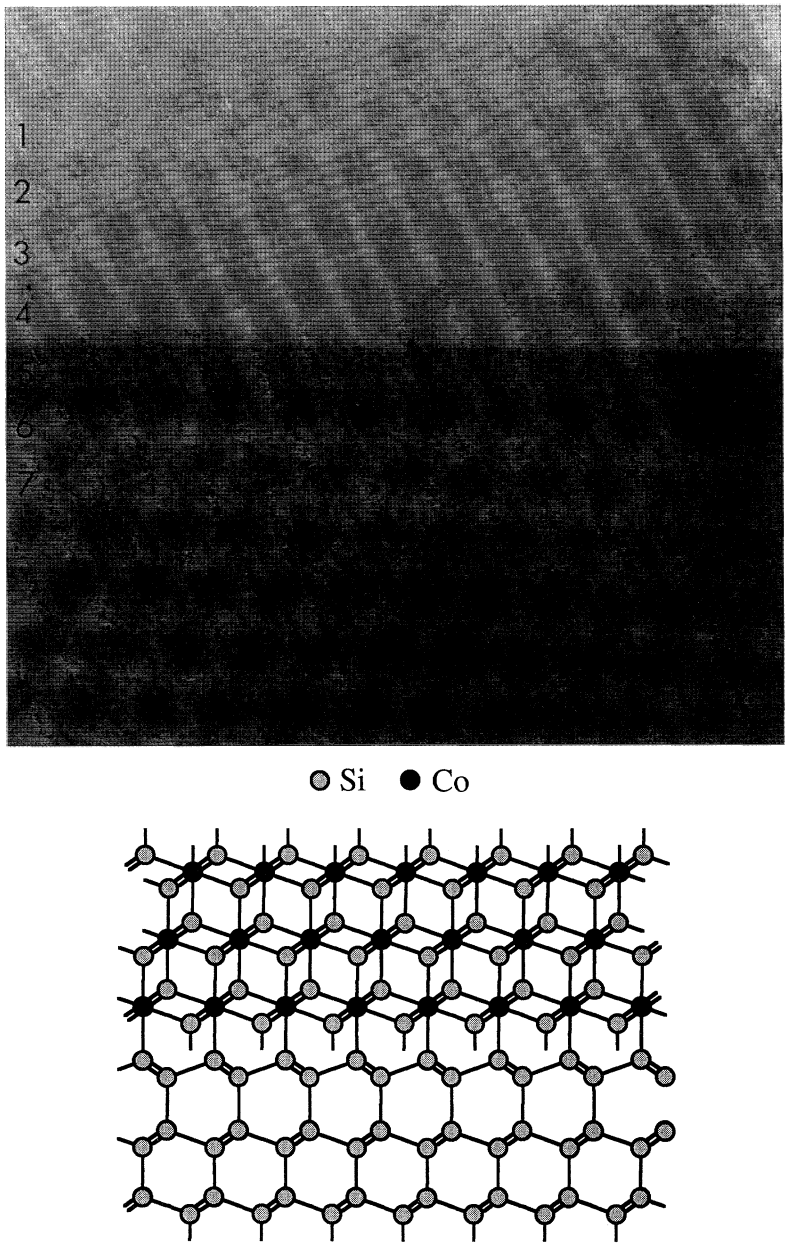

Figure 3. (*a*) *Z*-contrast image of an epitaxial $CoSi_2$–Si(111) interface, taken with the 100 kV microscope, showing direct determination of the interface structure (*b*).

needed to understand the image, unexpected interface structures will be appreciated immediately, while the specimen is still being viewed in the microscope, as apparent at the $CoSi_2$–Si(111) interface in figure 3 (Chisholm *et al.* 1994). Here the Co columns dominate the image from the $CoSi_2$, with the Si columns forming a bright background, while the dumbbells are seen in the Si substrate. The last plane of the Si is clearly seen to lie in a twinned orientation, and the structure model (figure 3*b*) can be drawn directly from the image.

Downloaded from rsta.royalsocietypublishing.org

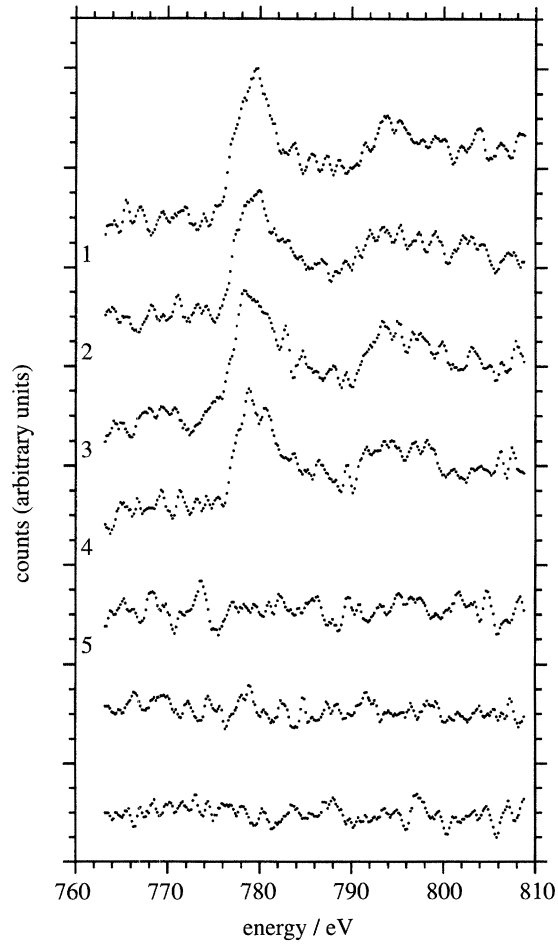

Figure 4. Co L spectra recorded plane by plane across the interface shown in figure 3, demonstrating atomic resolution analysis with a resolution of 2.7 Å.

This strategy is completely opposite to that of conventional high-resolution electron microscopy, where the goal is the precise measurement of phases. Here we attempt to destroy all phase correlations, except those depending on probe position, by integrating over the annular detector, which results in an image whose intensity is directly correlated with atomic column positions (Jesson & Pennycook 1993, 1995). In thicker crystals, the angular spread of the probe itself is an important contributor to the incoherent characteristics (Pennycook & Jesson 1990, 1991, 1992). The dynamical diffraction effects inherent in a conventional phase contrast image are averaged by this angular integration, and incoherent characteristics are retained. Physically, one can simply imagine that part of the probe channels along each column, and the remaining electrons do not contribute to the image contrast. The channelled fraction depends on the probe intensity at the top of the column, so as the probe scans the specimen is effectively illuminated atomic column by atomic column. Detecting incoherently generated elastic and inelastic scattering then leads to column-by-column imaging and column-by-column analysis.

For incoherent imaging conditions to apply with inelastically scattered electrons, they must also be collected over a large angular range (Ritchie & Howie 1988; Pen-

Downloaded from rsta.royalsocietypublishing.org

nycook *et al.* 1995). Since the inelastic scattering is forward peaked, it is possible to establish incoherent conditions for the elastic and inelastic signals simultaneously, while still collecting a substantial fraction of the total elastic and inelastic scattering. However, inelastic scattering events tend to be less localized to the atomic sites than elastic scattering events, and to achieve an atomic resolution analysis it becomes necessary to use quite high energy losses to enforce a local interaction. This means that the inelastic cross sections are much smaller than those for elastic scattering, too small to allow imaging with reasonable scan times. In this case, since incoherent conditions apply to both signals, the Z-contrast image can be used as a reference image to position the probe for atomic resolution spectroscopy (Browning *et al.* 1993*a*). Figure 4 shows spectra acquired in this way across the silicide interface of figure 3. Clearly the Co-L edge disappears on moving from the last plane of the silicide to the first plane of the silicon, demonstrating that atomic resolution chemical analysis is possible by such means. It should be noted that localized inelastic scattering only occurs with a large spectrometer acceptance aperture; for spatial resolution to be limited primarily by the probe the acceptance aperture should be significantly higher than the probe-forming aperture. One consequence of this, apparent in the spectra of figure 4, is that the width of the fine structure is degraded to about 5 eV due to the inclusion of non-dipole transitions at the higher scattering angles.

Atomic-sized probes necessarily have a rather low beam current, so to compensate for this, and avoid beam damage from long exposures, we use a highly efficient CCD detection system designed by McMullan *et al.* (1990). Nevertheless, exposures are still limited to a few seconds because of specimen drift or damage, resulting in detection sensitivities at the few % level. However, since only a few tens of atoms are contained in one atomic column, single atom detectability is expected for thin crystals. Dopants or impurities that segregate to some recognizable feature, such as a dislocation core, should be detectable below the level at which precipitation occurs. It may even prove feasible to map segregation atomic column by atomic column to reveal the dislocation core structure and its impurity atmosphere. Such data would represent a firm foundation for theoretical studies of the electronic effects of individual dislocations.

2. Direct structure inversion by maximum entropy

Incoherent imaging avoids the phase inversion problem of conventional structure determination methods, and therefore allows the direct retrieval of specimen structure. Given also the fact that we expect a discrete lattice of localized scatterers, a maximum entropy analysis is particularly attractive. We use software due to Gull & Skilling (1984) to retrieve the most likely object consistent with the image, assuming no prior knowledge of likely atom positions. The method requires a specified probe intensity profile, which represents the instrumental resolution function, and can best be estimated from the image itself. Knowledge of the exact microscope probe profile is not critical to the analysis, which is also robust towards specimen tilts and microscope misalignments, providing column coordinates with an accuracy of around 0.2 Å (McGibbon *et al.* 1996*a*). Figure 5 shows this procedure applied to a $SrTiO_3$ image obtained with the 100 kV STEM. Note that intensity information is preserved in the retrieved object, as shown in figure 5*b* where the Sr column locations are seen as brighter dots than the Ti columns. For presentational purposes this object can then be convoluted with a small Gaussian to give the reconstructed image shown in figure 5*c*.

Downloaded from rsta.royalsocietypublishing.org

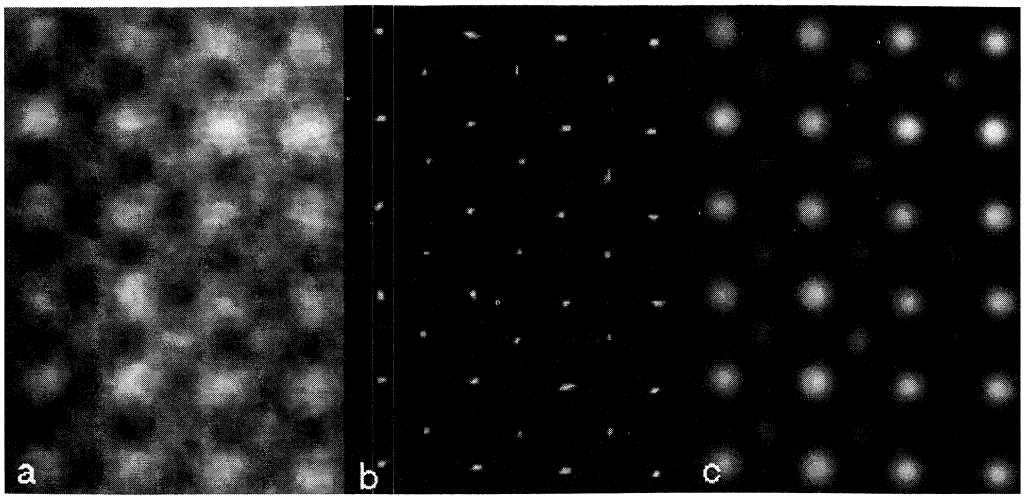

Figure 5. (*a*) *Z*-contrast image of $SrTiO_3$ viewed along the [001] direction; the brightest spots correspond to the Sr columns, separation 3.9 Å, the less bright spots are Ti–O columns. (*b*) Maximum entropy retrieval of the most likely object given only the probe profile. (*c*) Convolution of the retrieved object with a small Gaussian to form a noise-reduced maximum entropy image which retains the position and intensity information of the original image.

As seen in figures 2 and 3, the dumbbells in Si [110] are unresolved in 100 kV images, showing as a single elongated image feature. The maximum entropy method applied to such images will generate pairs of columns with the correct spacing, within the 0.2 Å statistical errors due to the shot noise (Pennycook *et al.* 1994). However, it is important to appreciate that accurate intensity information requires a higher information content in the raw image; for example, to distinguish the sublattice polarity in GaAs requires the use of a 300 kV STEM as shown below.

3. Determination of grain boundary structural units

These techniques make possible the determination of grain boundary structure models directly from the experimental data. As a demonstration of this capability, figure 6 shows the maximum entropy image of a 25° symmetric [001] tilt grain boundary in a $SrTiO_3$ bicrystal, obtained with the 100 kV STEM (McGibbon *et al.* 1994). The cation coordinates are determined from the maximum entropy analysis, while electron energy loss spectroscopy provides complementary information on the oxygen coordination (Brydson *et al.* 1992). Spectra recorded from the grain boundary plane showed no major departures from octahedral Ti–O coordination, though evidence of bond distortion was found. The O atoms were therefore placed in octahedral positions and the structure refined using bond valence sums (Altermatt & Brown 1985; Brown & Altermatt 1985) to give the final structure shown in figure 6*b*. In this refinement, it was not necessary to displace any column by more than the 0.2 Å inherent error in the maximum entropy object function. Although bond valence sums are not an energy minimization scheme, and cannot be used to predict structures from a selection of possible models, they do indicate the validity of a given structure, and in this sense they can validate the structure model deduced experimentally.

Several unexpected features were found at this grain boundary, most significantly, the presence of half-filled Sr columns which are shown hatched. The incoherent nature

Downloaded from rsta.royalsocietypublishing.org

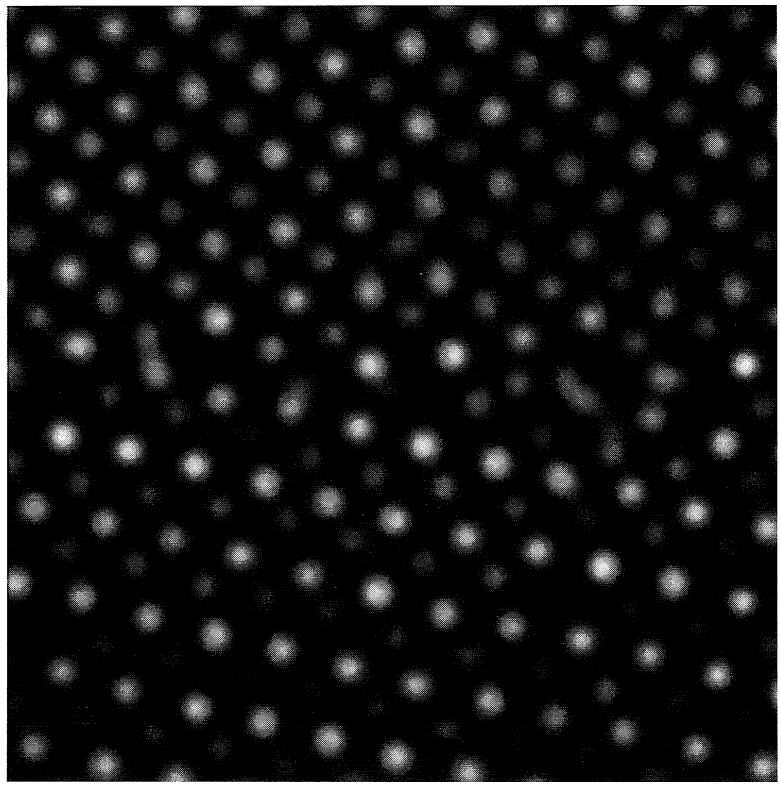

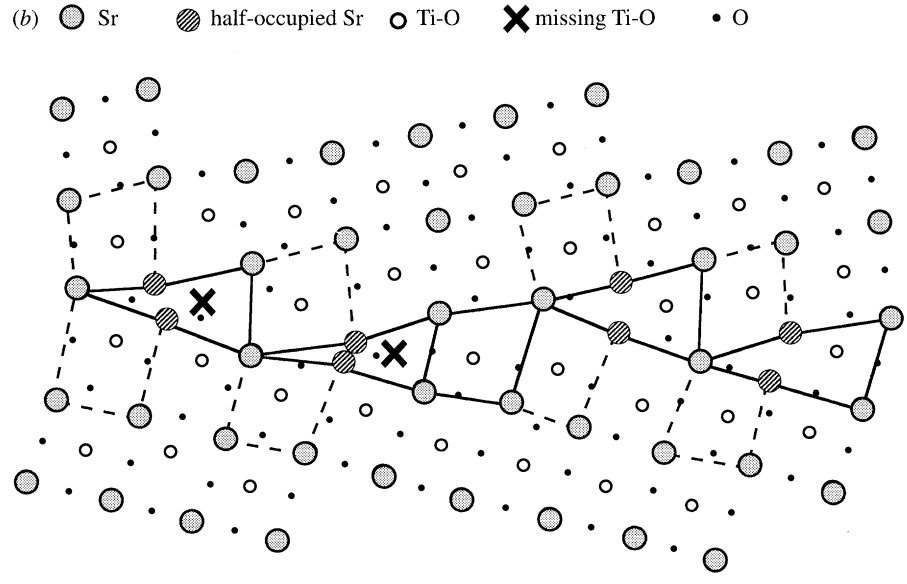

Figure 6. (*a*) Maximum entropy image of a 25° symmetric [001] tilt grain boundary in a $SrTiO_3$ bicrystal. (*b*) Deduced atomic structure. Note the microscopic asymmetry of the boundary structure.

of the Z-contrast image definitively indicates two scattering centres approximately 2 Å apart, both of which would appear to be Sr from their positions in their respective

PHILOSOPHICAL TRANSACTIONS OF THE ROYAL SOCIETY A MATHEMATICAL, PHYSICAL & ENGINEERING SCIENCES

PHILOSOPHICAL TRANSACTIONS OF THE ROYAL SOCIETY A MATHEMATICAL, PHYSICAL & ENGINEERING SCIENCES

Downloaded from rsta.royalsocietypublishing.org

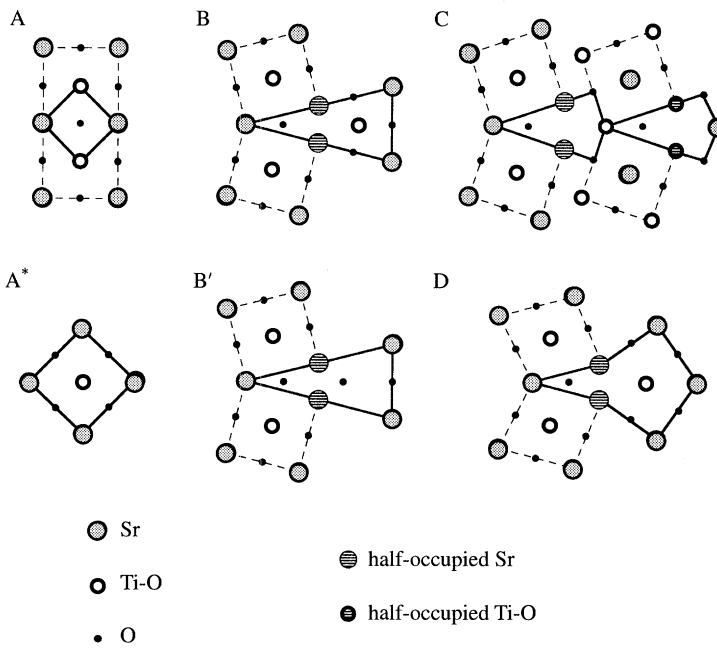

Figure 7. Structural units for symmetric [001] tilt grain boundaries in $SrTiO_3$ deduced from experimental data.

halves of the bicrystal, but clearly they cannot coexist at that spacing if both are fully occupied. The half columns, which can equally be regarded as a single zigzag column, represent a dislocation core reconstruction. This is the simplest structure model consistent with the experimental data. These columns do show reduced image intensity as would be expected, although quantification of intensities at the boundary plane is not sufficiently accurate to determine their precise occupancy due to static displacements and uncertainties in the atomic vibration amplitudes of atoms at the boundary.

The structural units comprising this {920} boundary are clearly triangular in form, and represent primitive dislocation cores. This is surprising because it introduces a microscopic asymmetry into the boundary structure, whereas macroscopically the bicrystal is symmetric. Furthermore, two variants of the basic structural unit were found, with and without a central Ti–O column. The reason for this is not clear, but relaxations of the neighboring cells correlated with the presence or absence of the Ti–O column. A relatively large expansion was measured normal to the boundary plane, 0.6 ± 0.2 Å. Together with the half columns this represents the grain boundary excess volume. One can also speculate on the likely atomic sites for impurity atoms; clearly, the Sr ions in the half-filled columns have a larger atomic volume than in the bulk, and so represent likely sites for substitution by large cations, while the relaxations around the Ti–O columns implies they could accomodate dopants of different valence.

Applying the same method to 36° and 65° symmetric tilt boundaries, further structural units were identified, again all characterized by the presence of half-filled columns (figure 7). It would appear that these half- or zigzag columns are quite ubiquitous. They certainly represent a rather simple solution to the classic problem of like-ion repulsion at grain boundaries in ionic materials, and may also be respon-

Downloaded from rsta.royalsocietypublishing.org

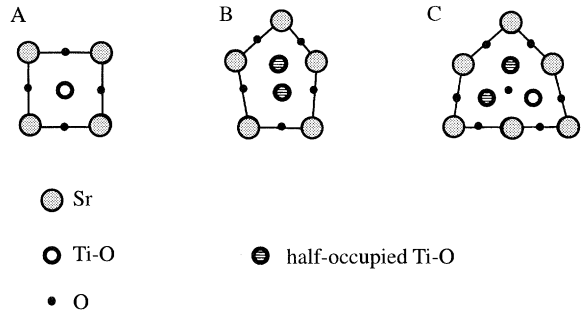

Figure 8. Structural units for asymmetric [001] tilt grain boundaries in $SrTiO_3$.

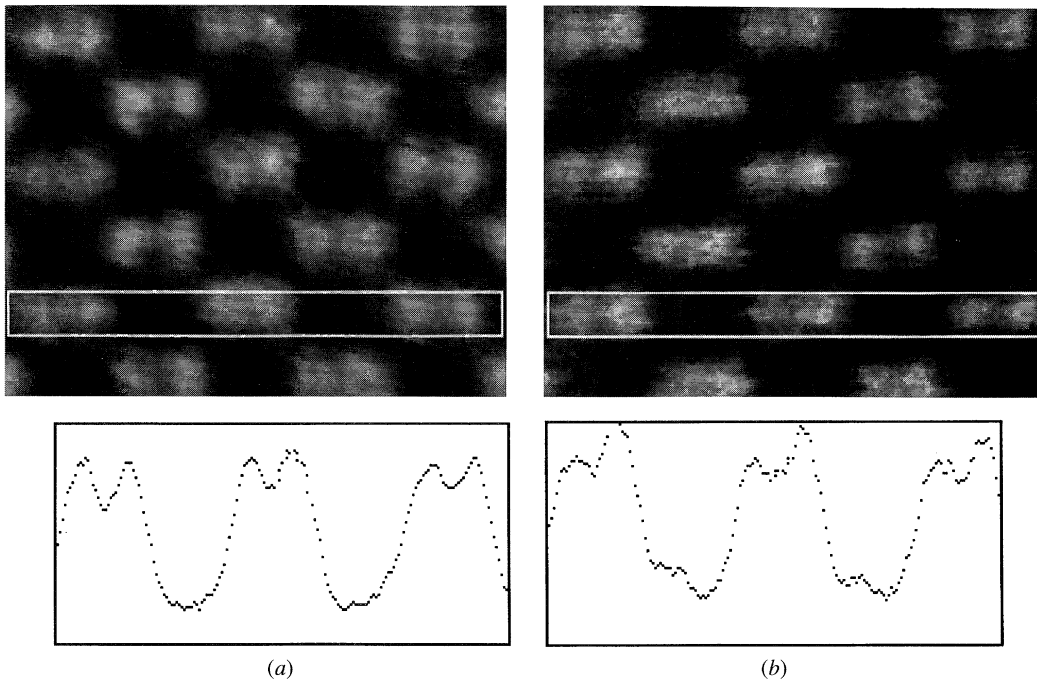

Figure 9. 300 kV Z-contrast images of (a) Si, and (b) GaAs line traces show vertically averaged intensity within the rectangles revealing lattice polarity.

sible for the indications of reduced occupancy at grain boundaries in other materials (Merkle & Smith 1987; Fonda *et al.* 1995).

For the 36° and 65° boundaries, the structural units were found to be non-primitive dislocation cores which preserve the microscopic symmetry of the boundary plane (figure 7). The changeover from primitive to non-primitive units can be explained by a simple application of linear elasticity theory (Browning *et al.* 1995). These additional structural units were sufficient to construct models for any symmetric [001] tilt grain boundary by the method of Sutton & Vitek (1983), suggesting that continuity of boundary structure might apply in this system. However, on testing this prediction with a 45° symmetric bicrystal it was found that the boundary had decomposed into a set of small asymmetric facets along the ⟨100⟩ and ⟨110⟩ directions. This would indicate that long period symmetric grain boundaries are energetically unstable as also suggested from the observations of Merkle & Wolf (1992). Again, however, two

Downloaded from rsta.royalsocietypublishing.org

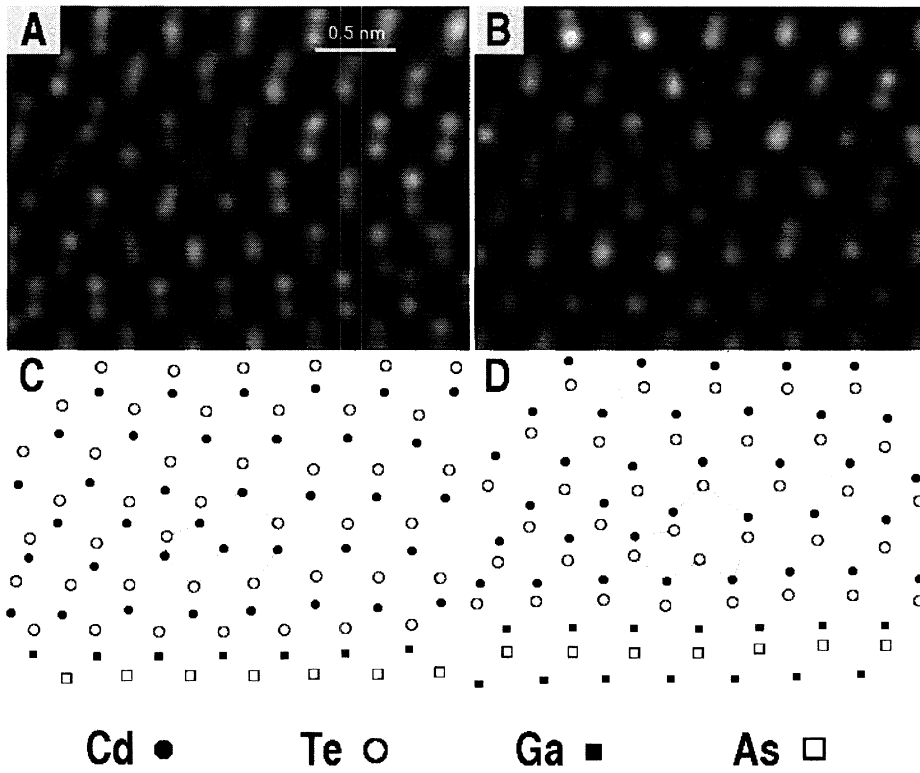

Figure 10. Maximum entropy images of 60° dislocations at the CdTe(001)–GaAs(001) interface viewed in (*a*) [1$\bar{1}$0] and (*b*) [110] orientations, with schematic representations given in (*c*) and (*d*), respectively. It can be seen that both dislocations are of the glide set, and are located a few monolayers above the interface.

distinct structural units could be identified, one of which was also seen in images from asymmetric facets present in the 24° grain boundary. Since two types of dislocation core are needed to describe an asymmetric grain boundary, it is clear that extended segments of boundary must comprise at least two units, and structure models can again be constructed for any asymmetric [001] tilt grain boundary by application of the method of Sutton & Vitek (1983) in two stages, one for each type of dislocation core (McGibbon 1995). These two units coexist over the entire misorientation range, with different frequencies relative to the spacer unit cells (figure 8).

Such an approach, combining *Z*-contrast imaging with EELS analysis, is equally applicable to other systems. With high-temperature superconductors for example, the hole concentration can be measured directly by EELS, without having to cool the specimen, with a spatial resolution below the superconducting coherence length (Browning *et al.* 1993*b*). This allows the local superconducting properties to be correlated with the actual atomic structure; preliminary results have demonstrated strong hole depletion at an asymmetric boundary, whereas none was observed at a symmetric boundary. Such effects may well be explained by the structural unit approach.

The same strategy will be applicable to semiconductor grain boundaries. However, the projected intercolumn spacings in these materials can be as small as 1.36 Å, so that determination of dislocation core structures requires the higher resolution of the 300 kV STEM.

Downloaded from rsta.royalsocietypublishing.org

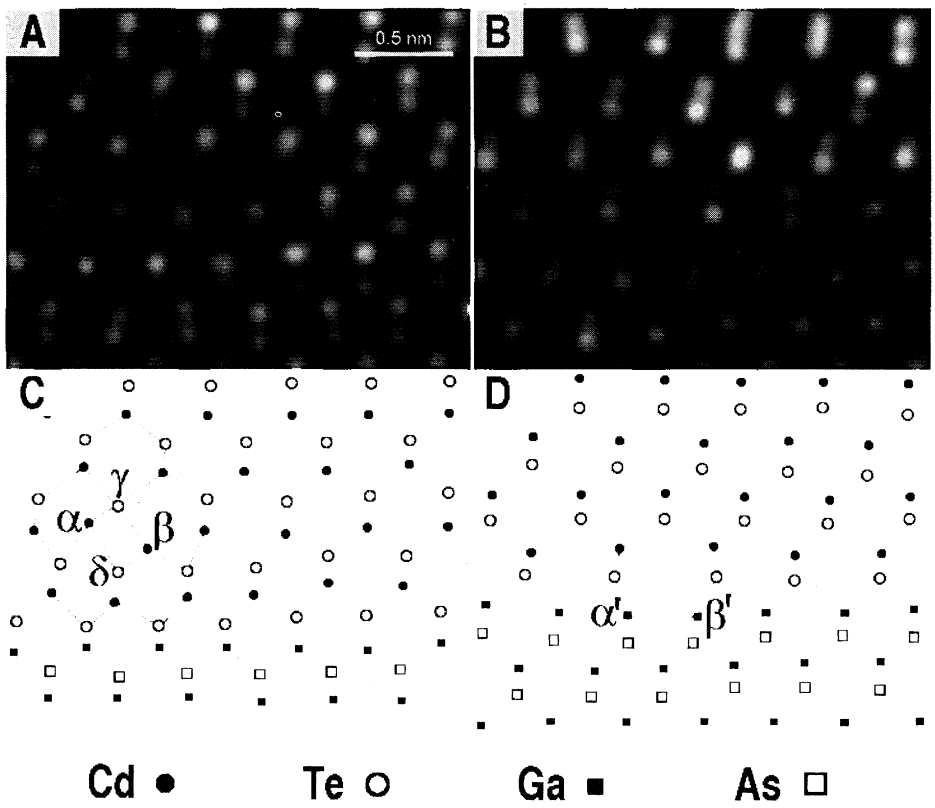

Figure 11. Lomer dislocations at the interface of CdTe(001)–GaAs(001) viewed in the (*a*) [1$\bar{1}$0] and (*b*) [110] orientations, with schematic representations given in (*c*) and (*d*), respectively. The dislocation in (*a*) lies a few monolayers above the interface and possesses an unexpected core structure while that in (*b*) lies at the interface and has the Hornstra structure.

4. Direct determination of misfit dislocation core structures in semiconductor heterostructures

A major motivation for a 300 kV STEM is the possibility of directly resolving and distinguishing the sublattice in compound semiconductors. Figure 8 compares maximum entropy images from Si and from GaAs in which the sublattice polarity is clearly visible. GaAs represents the most severe test, since Ga and As are only two atomic numbers apart, although they are expected to show $\sim$ 10% intensity difference which is sufficient to allow the polarity to be distinguished. At present, due to shot noise, image statistics limit the accuracy of intensity measurements and occasionally individual dumbbells are seen with inverted polarity. Thus a polarity determination requires more than one individual dumbbell.

Nevertheless, it is possible to determine the core structures of misfit dislocations in compound semiconductor heterostructures directly from such images. The lattice polarity is deduced several dumbbells away from the dislocation core, then compositions within the core region can be assigned by tracing out from the core to where the sublattice is known. In this way it has proved possible to distinguish glide and shuffle dislocations directly, and to determine the terminating species in the core (McGibbon *et al.* 1995). Figure 10 shows core structures of 60° dislocations at a CdTe–GaAs (001) interface, in the two perpendicular ⟨110⟩ directions. Both disloca-

Downloaded from rsta.royalsocietypublishing.org

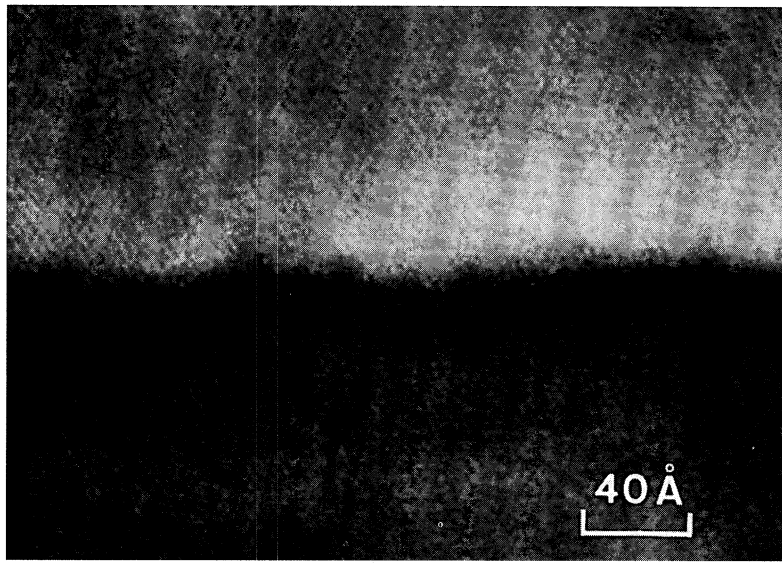

Figure 12. *Z*-contrast image of a GaAs–Si interface revealing nm-scale interfacial roughness.

tions are seen to be of glide type, one terminating at the Cd column, the other at the Te column. Figure 11 shows images of perfect edge (Lomer) dislocations from the same specimen, also in the two perpendicular ⟨110⟩ directions, one showing a core structure similar to that proposed originally by Hornstra (1958), the other showing an unexpected core structure comprising a four-fold ring surrounded by distorted six-fold rings. Only the Hornstra core is located at the interface plane; all others are located a few monolayers into the CdTe film. It can be speculated that the more polar CdTe does not like the five- or seven-membered rings of the Hornstra core. When the Hornstra core occurs, the like-ion bonds are Ga–Ga bonds, although the preference for one core structure over another can only become clear after theoretical investigations of the energetics of these structures. Certainly images such as these do have the power to reveal unanticipated effects; they do therefore represent firm starting points for theoretical studies of this nature.

5. Determination of interfacial roughness

Electron microscopy provides a two-dimensional projection of a three-dimensional structure. It is most effective in situations such as those described above, where the features of interest are aligned parallel to the beam direction. This limitation is not as severe as it might seem, since crystalline systems often facet onto crystallographic planes on a small scale, when good projections can be obtained in thin specimens. In many cases, the structure is clear from a single projection, although if necessary it would be possible to take images along different zone axis directions parallel to the interface to determine the three-dimensional structure.

Distinguishing small scale interfacial roughness from interdiffusion presents a substantial challenge for any structure determination method. The characteristics of incoherent imaging offer some potential in this regard, as illustrated by the *Z*-contrast image of a GaAs–Si(100) interface in figure 12 (Takasuka *et al.* 1992). The *Z*-contrast image maintains compositional sensitivity over a wide range of thickness. On the right side of the figure the specimen is thicker (image intensities are higher) and the in-

PHILOSOPHICAL TRANSACTIONS OF THE ROYAL SOCIETY A MATHEMATICAL, PHYSICAL & ENGINEERING SCIENCES
PHILOSOPHICAL TRANSACTIONS OF THE ROYAL SOCIETY A MATHEMATICAL, PHYSICAL & ENGINEERING SCIENCES

Downloaded from rsta.royalsocietypublishing.org

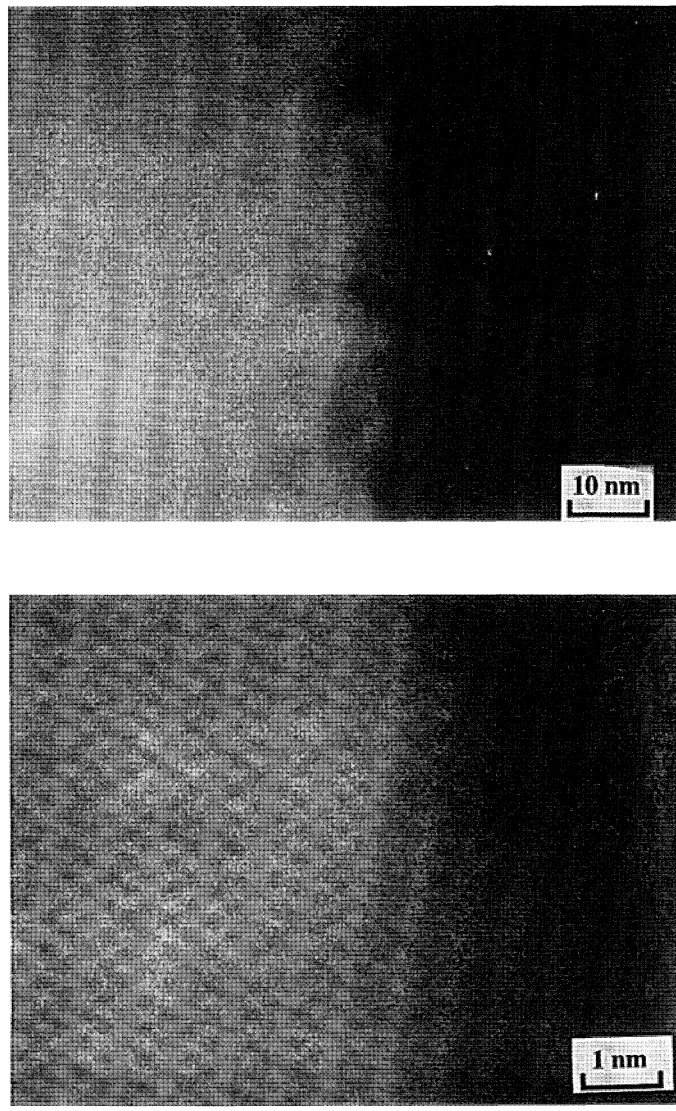

Figure 13. Z-contrast image of an amorphous–crystalline interface in ion-implanted Si (100): (a) low magnification view showing 10 nm scale roughness; (b) high magnification image showing individual dumbbells.

terface apears diffuse, consistent with either interdiffusion or small scale roughness. On the left-hand side, where the specimen is thinner, the interface is clearly seen to be rough, on the scale of a few nm. It is because Z-contrast imaging maintains compositional sensitivity even in the thinnest regions that the degree of roughness can be immediately appreciated.

Another example of a rough interface is shown in figure 13, an interface between crystalline and amorphous Si formed by ion implantation (150 keV Si^+ ions to a dose of 2×10^{15} cm^{-2} at liquid nitrogen temperature). The crystalline Si is oriented to its $\langle 110 \rangle$ axis and shows bright due to the strong axial channelling effect. The 10 nm scale of the interfacial roughness is again immediately apparent in areas that have a thickness of similar order. The roughness is also visible at higher magnifica-

Downloaded from rsta.royalsocietypublishing.org

tion where individual dumbbells are visible. It would be possible to quantify such information since the column intensity will be dependent on column length in a predictable and monatonic manner (Jesson & Pennycook 1995), allowing one to obtain the average dimensions of crystalline protuberances into the amorphous region, both perpendicular and parallel to the electron beam direction.

6. Summary

The advances of the last few years have now given us the tools with which to probe electronic materials at the true atomic scale, atomic column by atomic column, not only intrinsic structures such as dislocation cores, but also the nature and distribution of impurity segregation. The 1.3 Å probe of the 300 kV STEM means that all semiconductor materials can now be studied in a number of different orientations. It would be possible, for example, to examine a range of Si bicrystals to determine the grain boundary structural units, and dopant segregation could be investigated with EELS. In conjunction with theoretical modelling, it is certainly conceivable that an atomic level understanding of the fast diffusion paths in polycrystalline Si could now be developed.

This ability to correlate atomic structure with impurity segregation, in favorable cases being able to determine the impurity charge state, is expected to lead to new insights into many semiconducting materials issues, including gettering, diffusion and metallization. In conjunction with theoretical modelling it may lead finally to an atomic level understanding of the electronic and optical properties of semiconductor materials.

The authors are grateful to R. Jebasinski, S. Mantl, V. P. Dravid, V. Ravikumar and J. E. Angelo for provision of samples, and to T. C. Estes, J. T. Luck and S. L. Carney for technical assistance. This research was sponsored by the Division of Materials Sciences, U.S. Department of Energy, under contract DE–AC05–84OR21400 with Martin Marietta Energy Systems, Inc. and in part by appointments to the Oak Ridge National Laboratory Postdoctoral Research Program administered by the Oak Ridge Institute for Science and Education.

References

Altermatt, D. & Brown, I. D. 1985 The automatic searching for chemical bonds in inorganic crystal structures. *Acta Crystallogr.* B **41**, 240–244.

Brown, I. D. & Altermatt, D. 1985 Bond-valence parameters obtained from a systematic analysis of the inorganic crystal structure database. *Acta Crystallogr.* B **41**, 244–247.

Browning, N. D., Chisholm, M. F. & Pennycook, S. J. 1993*a* Atomic-resolution chemical analysis using a scanning transmission electron microscope. *Nature* **366**, 143–146.

Browning, N. D., Chisholm, M. F., Pennycook, S. J., Norton, D. P. & Lowndes, D. H. 1993*b* Correlation between hole depletion and atomic structure at high-angle grain boundaries in $YBa_2Cu_3O_{7-\delta}$. *Physica* **C212**, 185–190.

Browning, N. D., Pennycook, S. J., Chisholm, M. F., McGibbon, M. M. & McGibbon, A. J. 1995 Observation of structural units at symmetric [001] tilt boundaries in $SrTiO_3$. *Interf. Sci.* **2**, 397–423.

Brydson, R., Sauer, H. & Engel, W. 1992 Electron energy loss near-edge structure as an analytical tool—the study of minerals. In *Transmission electron energy loss spectrometry in materials science* (ed. M. M. Disko, C. C. Ahn & B. Fultz), pp. 131–154. The Minerals, Metals & Materials Society.

Chisholm, M. F., Pennycook, S. J., Jebasinski, R. & Mantl, S. 1994 New interface structure for A-Type $CoSi_2$/Si(111). *Appl. Phys. Lett.* **64**, 2409–2411.

PHILOSOPHICAL TRANSACTIONS OF THE ROYAL SOCIETY A MATHEMATICAL, PHYSICAL & ENGINEERING SCIENCES

PHILOSOPHICAL TRANSACTIONS OF THE ROYAL SOCIETY A MATHEMATICAL, PHYSICAL & ENGINEERING SCIENCES

Downloaded from rsta.royalsocietypublishing.org

Crewe, A. V. 1980 The physics of the high-resolution scanning microscope. *Rep. Prog. Phys.* **43**, 621–639.

Crewe, A. V. & Wall, J. 1970 A scanning microscope with 5 Å resolution. *J. Molec. Biol.* **48**, 375–393.

Crewe, A. V., Wall, J. & Langmore, J. 1970 Visibility of single atoms. *Science* **168**, 1338–1340.

Engel, A., Wiggins, J. W. & Woodruff, D. C. 1974 A comparison of calculated images generated by six modes of transmission electron microscopy. *J. Appl. Phys.* **45**, 2739–2747.

Fonda, R. W., Yan, M. & Luzzi, D. E. 1995 Atomic structure of the $\Sigma = 5$, (310) [001] grain boundary in NiAl: a combined electron microscopy and theoretical study. *Phil. Mag. Lett.* **71**, 221–228.

Gull, S. F. & Skilling, J. 1984 Maximum entropy method in image processing. *IEE Proc.* **131**, 646–659.

Hornstra, J. 1958 Dislocations in the diamond lattice. *J. Phys. Chem. Solids* **5**, 129–141.

Jesson, D. J. & Pennycook, S. J. 1993 Incoherent imaging of thin specimens using coherently scattered electrons. *Proc. R. Soc. Lond.* A **441**, 261–281.

Jesson, D. J. & Pennycook, S. J. 1995 Incoherent imaging of crystals using thermally scattered electrons. *Proc. R. Soc. Lond.* A **449**, 273–293.

McGibbon, M. M., Browning, N. D., Chisholm, M. F., McGibbon, A. J., Pennycook, S. J., Ravikumar, V. & Dravid, V. P. 1994 Direct determination of grain boundary atomic structure in $SrTiO_3$. *Science* **266**, 102–104.

McGibbon, M. M., Browning, N. D., McGibbon, A. J. & Pennycook, S. J. 1996*b* *Phil. Mag.* A **73**, 625–641.

McGibbon, A. J., Pennycook, S. J. & Angelo, J. E. 1995 Direct observation of dislocation core structures in CdTe/CdTe (001). *Science* **269**, 519–521.

McGibbon, A. J., Pennycook, S. J. & Jesson, D. E. 1996*a* Crystal structure retrieval by maximum entropy analysis of atomic-resolution incoherent images. *J. Microscopy.* (In the press.)

McMullan, D., Rodenburg, J. M., Murooka, Y. & McGibbon, A. J. 1990 Parallel EELS CCD detector for a VG HB501 STEM. *IOP Conf. Series* **98**, 55–58.

Merkle, K. L. & Smith, D. J. 1987 Atomic structure of symmetric tilt grain boundaries in NiO. *Phys. Rev. Lett.* **59**, 2887–2890.

Merkle, K. L. & Wolf, D. 1992 Low-energy configurations of symmetric and asymmetric tilt grain boundaries. *Phil. Mag.* A **65**, 513–530.

Pennycook, S. J. & Jesson, D. E. 1990 High-resolution incoherent imaging of crystals. *Phys. Rev. Lett.* **64**, 938–941.

Pennycook, S. J. & Jesson, D. E. 1991 High-resolution Z-contrast imaging of crystals. *Ultramicroscopy* **37**, 14–38.

Pennycook, S. J. & Jesson, D. E. 1992 Atomic-resolution Z-contrast imaging of interfaces. *Acta Metall. Mater.* **40**, S149–S159.

Pennycook, S. J., Browning, N. D., Jesson, D. E., Chisholm, M. F. & McGibbon, A. J. 1993 Atomic-resolution imaging and spectroscopy of semiconductor interfaces. *Appl. Phys.* A **57**, 385–391.

Pennycook, S. J., Jesson, D. E., Chisholm, M. F., Ferridge, A. G. & Seddon, M. J. 1994 Sub-ångström microscopy through incoherent imaging and image reconstruction. In *Proc. 10th Pfefferkorn Conf. on Signal and Image Processing* (ed. O. Johari), pp. 233–242. Chicago, IL: Scanning Microscopy International.

Pennycook, S. J., Jesson, D. E. & Browning, N. D. 1995 Atomic-resolution electron energy loss spectroscopy in crystalline solids. *Nucl. Instrum. Methods Phys. Res.* B **96**, 575–582.

Ritchie, R. H. & Howie, A. 1988 Inelastic scattering probabilities in scanning transmission electron microscopy. *Phil. Mag.* A **58**, 753–767.

Sutton, A. P. & Vitek, V. 1983 On the structure of tilt grain boundaries in cubic metals. I. Symmetric tilt boundaries. *Phil. Trans. R. Soc. Lond.* A **309**, 1–36.

Takasuka, E., Asai, K., Fujita, K., Chisholm, M. F. & Pennycook, S. J. 1992 High-resolution Z-contrast observation of GaAs/Si hetero-interfaces through scanning transmission electron microscope. *Jap. J. Appl. Phys.* **31**, L1788–L1790.

PHILOSOPHICAL TRANSACTIONS OF THE ROYAL SOCIETY A MATHEMATICAL, PHYSICAL & ENGINEERING SCIENCES

PHILOSOPHICAL TRANSACTIONS OF THE ROYAL SOCIETY A MATHEMATICAL, PHYSICAL & ENGINEERING SCIENCES

Downloaded from rsta.royalsocietypublishing.org

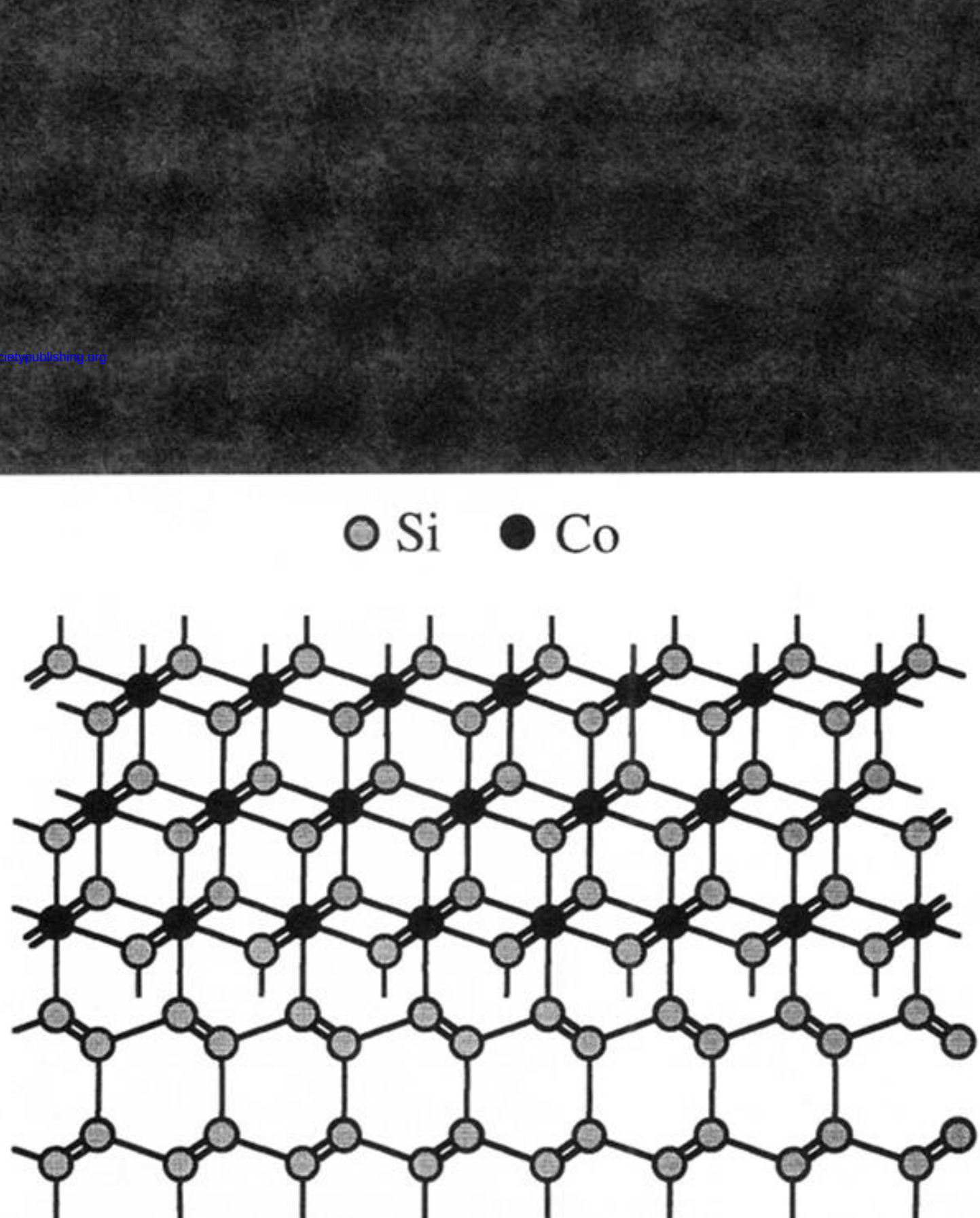

gure 3. (*a*) *Z*-contrast image of an epitaxial $CoSi_2$–Si(111) interface, taken with the 100 kV microscope, showing direct determination of the interface structure (*b*).

PHILOSOPHICAL TRANSACTIONS OF THE ROYAL SOCIETY A MATHEMATICAL, PHYSICAL & ENGINEERING SCIENCES

Downloaded from rsta.royalsocietypublishing.org

PHILOSOPHICAL TRANSACTIONS OF THE ROYAL SOCIETY A MATHEMATICAL, PHYSICAL & ENGINEERING SCIENCES

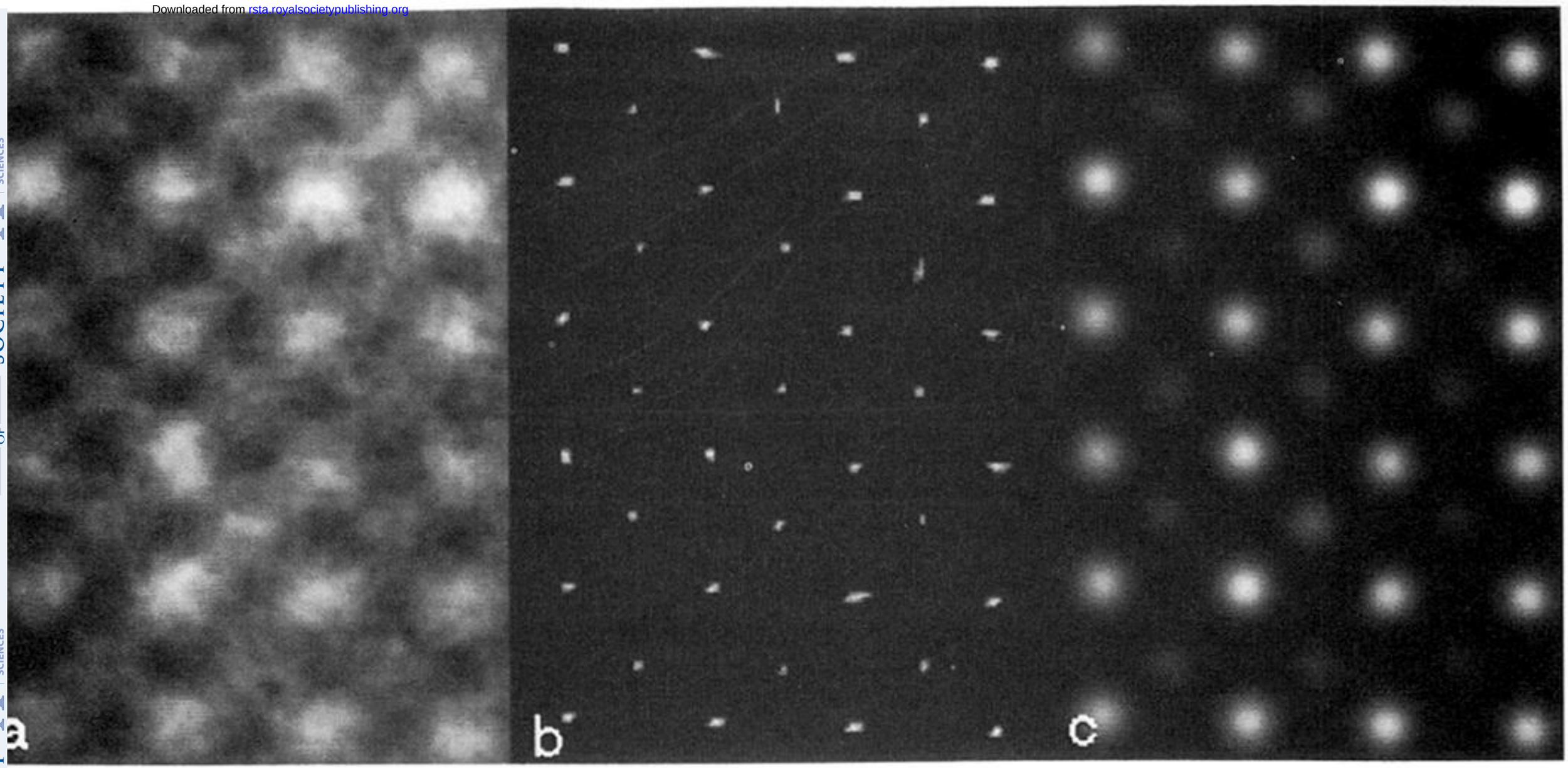

igure 5. (a) Z-contrast image of $SrTiO_3$ viewed along the [001] direction; the brightest spots orrespond to the Sr columns, separation 3.9 Å, the less bright spots are Ti–O columns. (b) laximum entropy retrieval of the most likely object given only the probe profile. (c) Convolution f the retrieved object with a small Gaussian to form a noise-reduced maximum entropy image hich retains the position and intensity information of the original image.

Downloaded from rsta.royalsocietypublishing.org

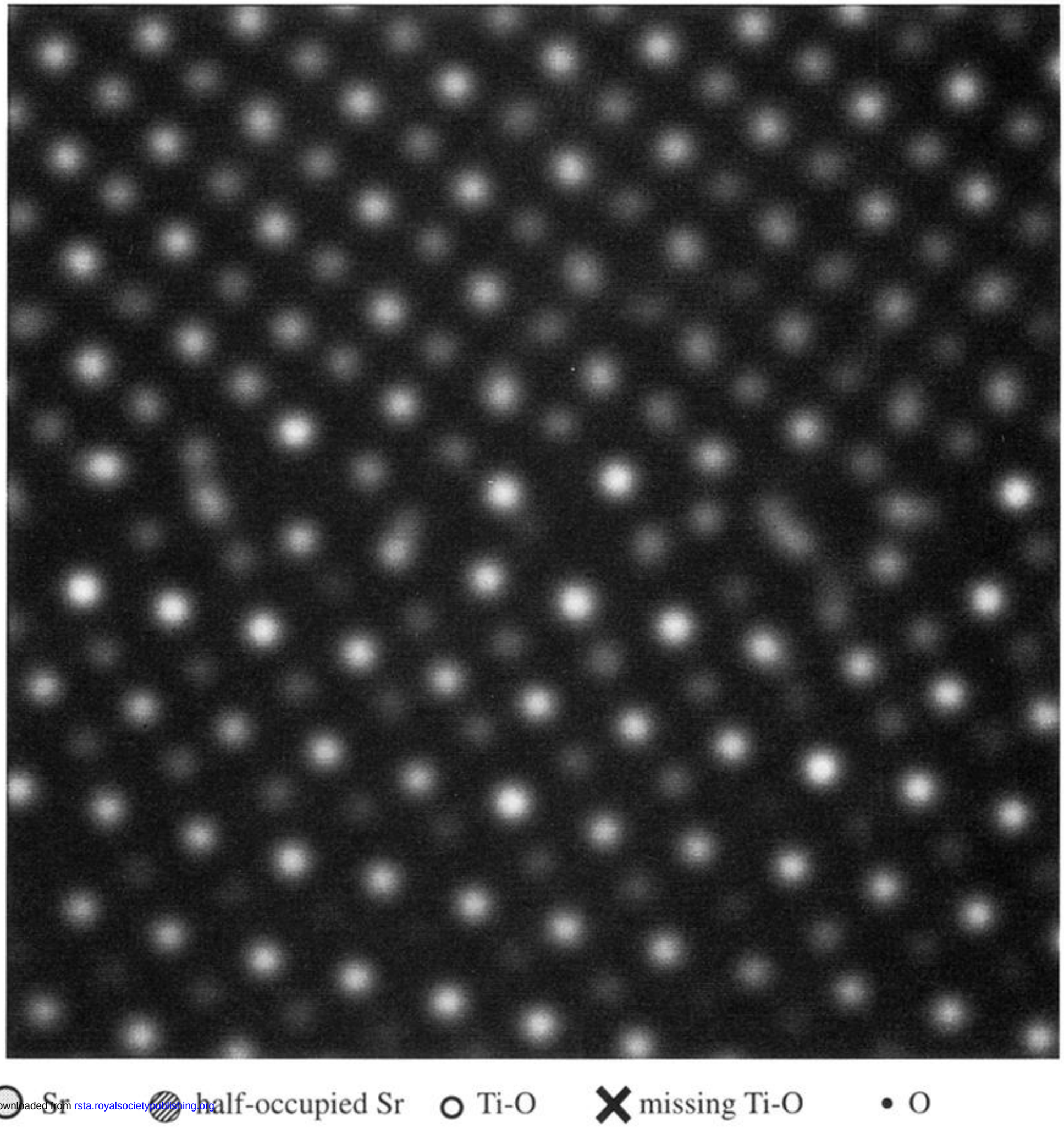

Figure 6. (*a*) Maximum entropy image of a 25° symmetric [001] tilt grain boundary in a $SrTiO_3$ crystal. (*b*) Deduced atomic structure. Note the microscopic asymmetry of the boundary structure.

PHILOSOPHICAL TRANSACTIONS OF THE ROYAL SOCIETY A MATHEMATICAL, PHYSICAL & ENGINEERING SCIENCES

Downloaded from rsta.royalsocietypublishing.org

PHILOSOPHICAL TRANSACTIONS OF THE ROYAL SOCIETY A MATHEMATICAL, PHYSICAL & ENGINEERING SCIENCES

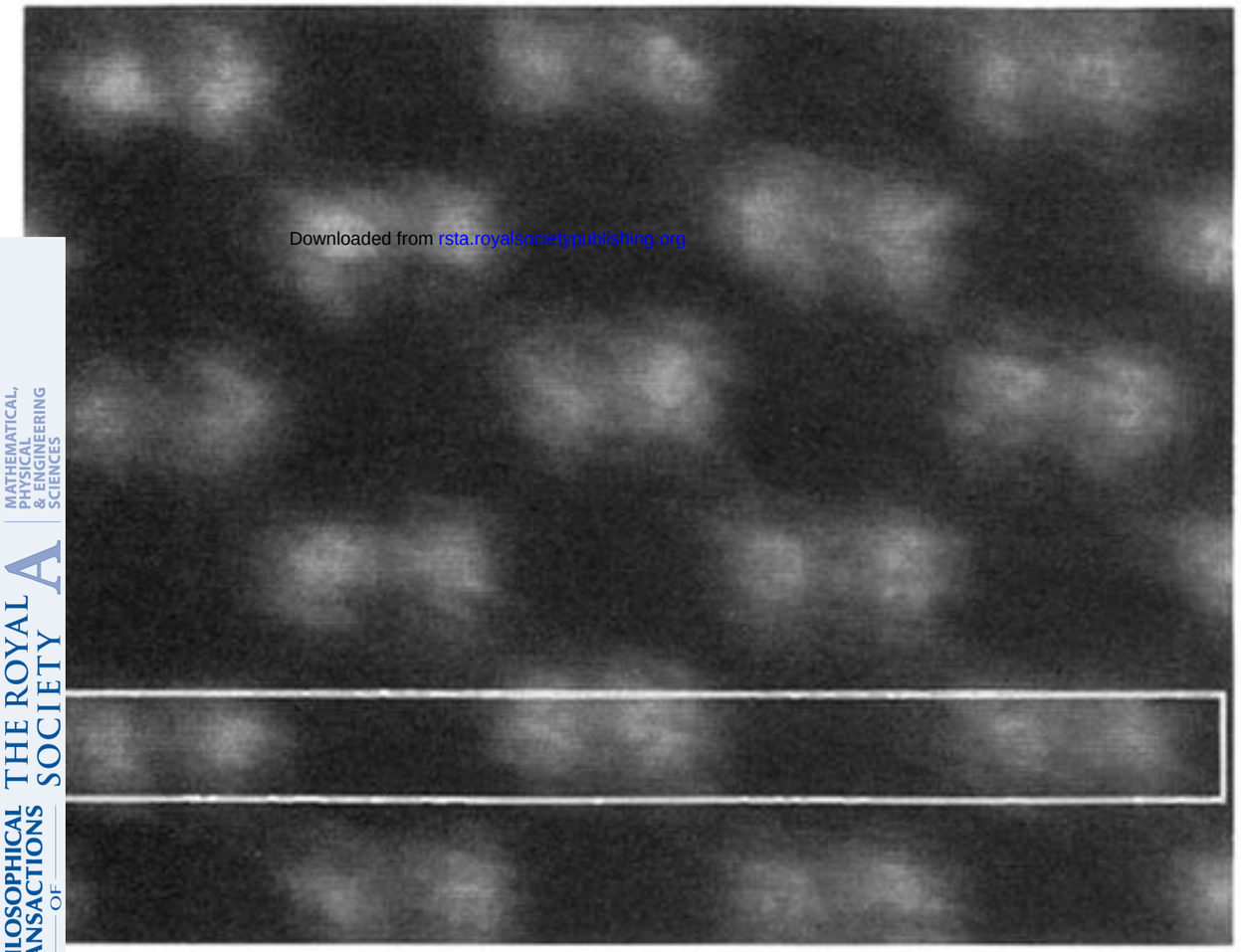

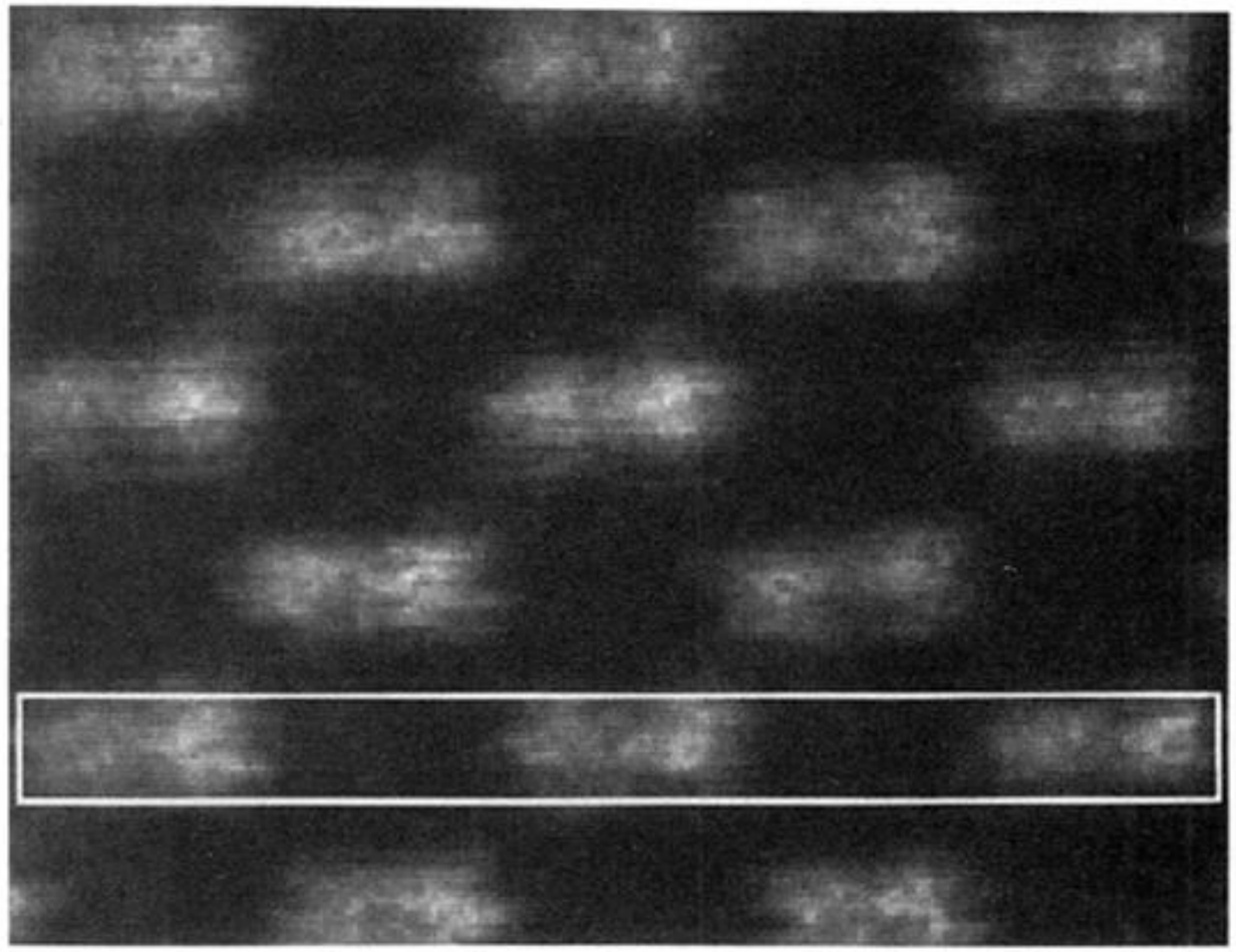

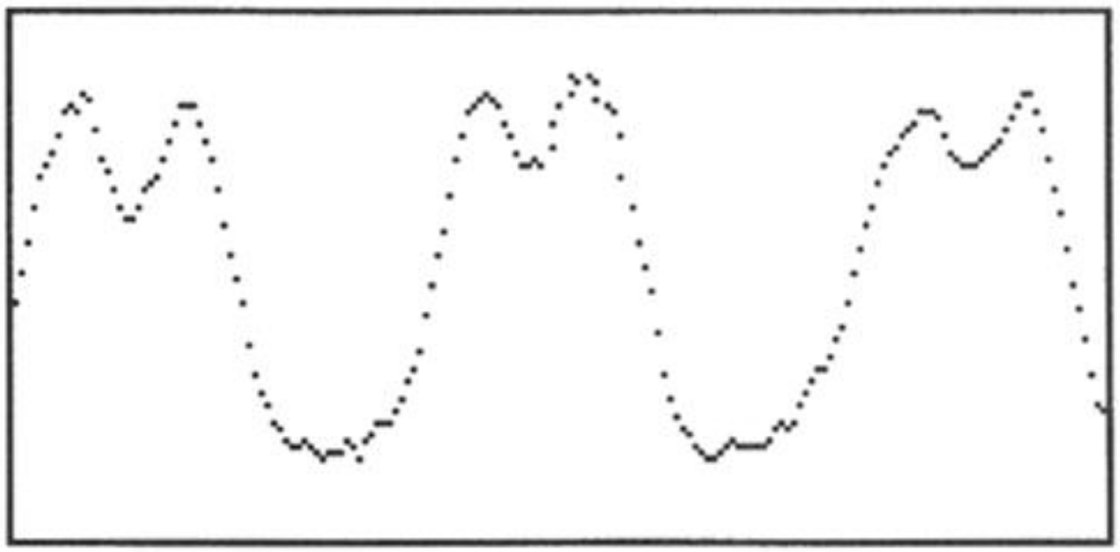

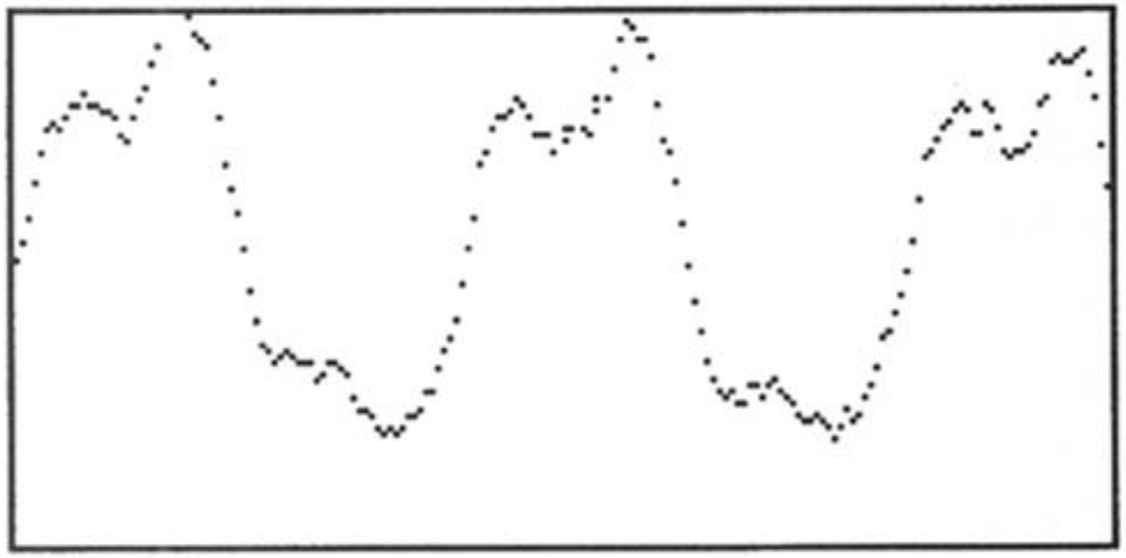

(*a*) (*b*)

Figure 9. 300 kV *Z*-contrast images of (*a*) Si, and (*b*) GaAs line traces show vertically averaged intensity within the rectangles revealing lattice polarity.

Downloaded from rsta.royalsocietypublishing.org

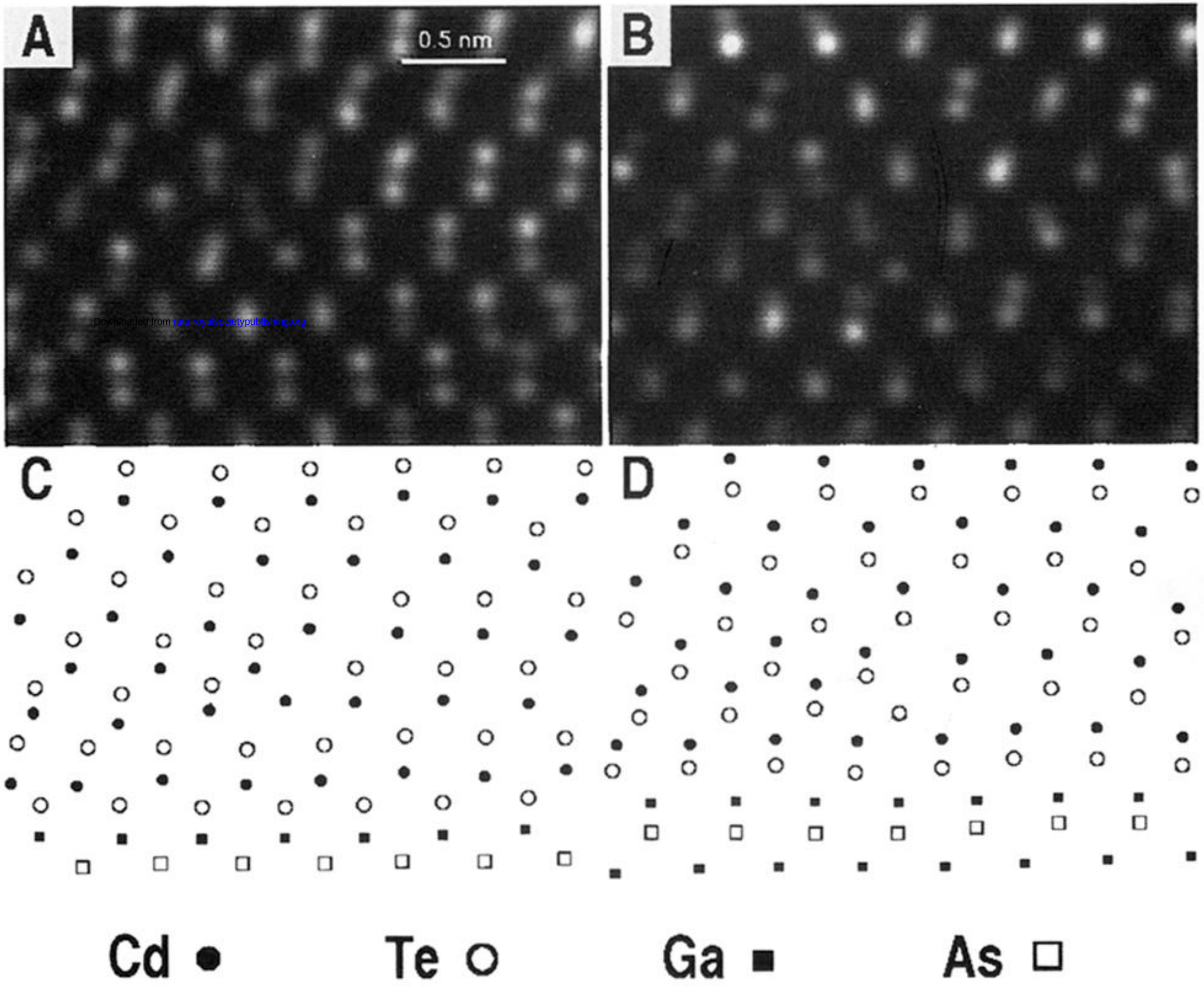

igure 10. Maximum entropy images of 60° dislocations at the CdTe(001)–GaAs(001) interface ewed in (*a*) [1$\bar{1}$0] and (*b*) [110] orientations, with schematic representations given in (*c*) and !), respectively. It can be seen that both dislocations are of the glide set, and are located a few onolayers above the interface.

PHILOSOPHICAL TRANSACTIONS OF THE ROYAL SOCIETY A MATHEMATICAL, PHYSICAL & ENGINEERING SCIENCES
PHILOSOPHICAL TRANSACTIONS OF THE ROYAL SOCIETY A MATHEMATICAL, PHYSICAL & ENGINEERING SCIENCES

Downloaded from rsta.royalsocietypublishing.org

gure 11. Lomer dislocations at the interface of CdTe(001)–GaAs(001) viewed in the (*a*) [1$\bar{1}$0] nd (*b*) [110] orientations, with schematic representations given in (*c*) and (*d*), respectively. The slocation in (*a*) lies a few monolayers above the interface and possesses an unexpected core ructure while that in (*b*) lies at the interface and has the Hornstra structure.

PHILOSOPHICAL TRANSACTIONS OF THE ROYAL SOCIETY A MATHEMATICAL, PHYSICAL & ENGINEERING SCIENCES

PHILOSOPHICAL TRANSACTIONS OF THE ROYAL SOCIETY A MATHEMATICAL, PHYSICAL & ENGINEERING SCIENCES

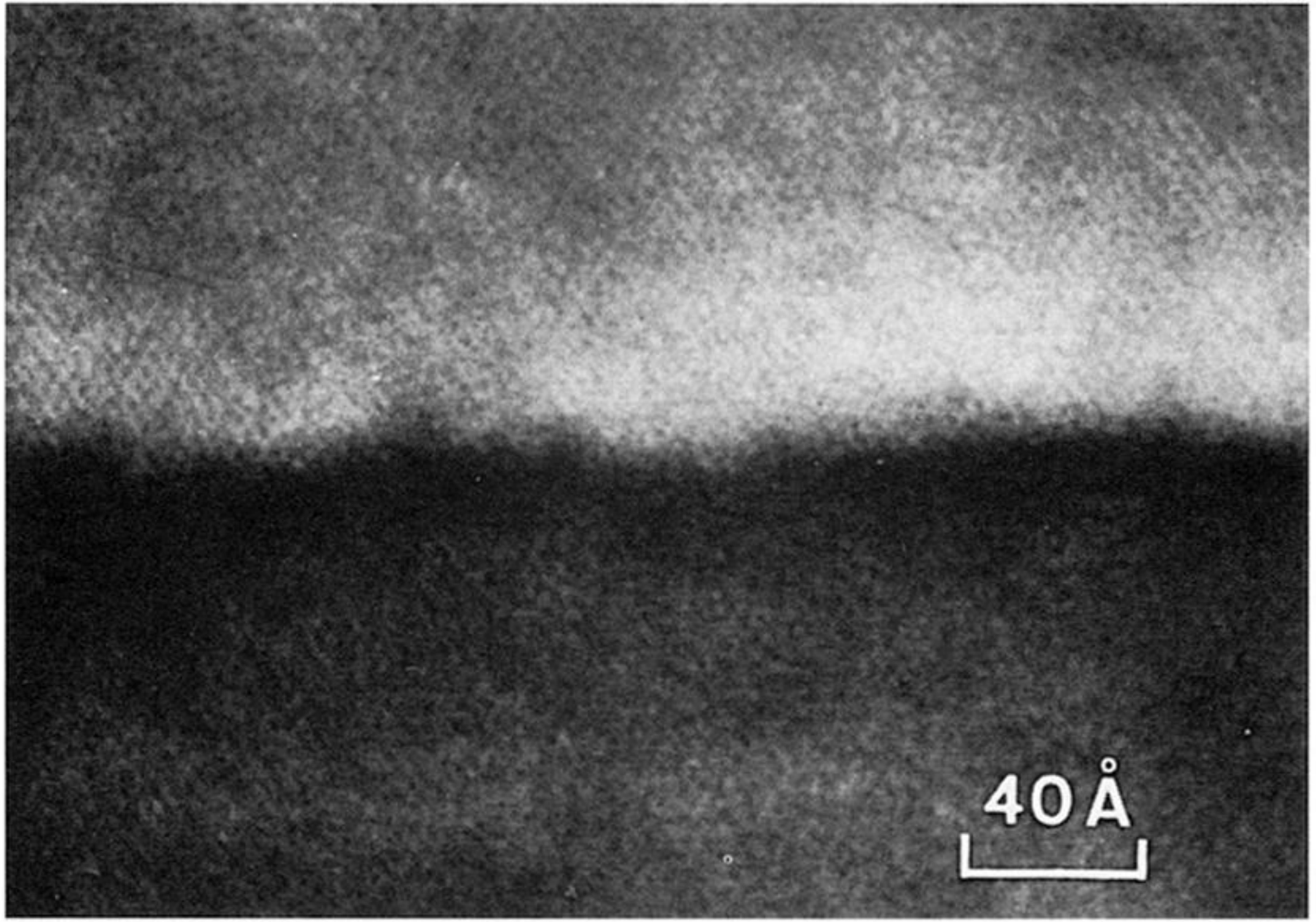

igure 12. Z-contrast image of a GaAs–Si interface revealing nm-scale interfacial roughness.

PHILOSOPHICAL TRANSACTIONS OF THE ROYAL SOCIETY A MATHEMATICAL, PHYSICAL & ENGINEERING SCIENCES

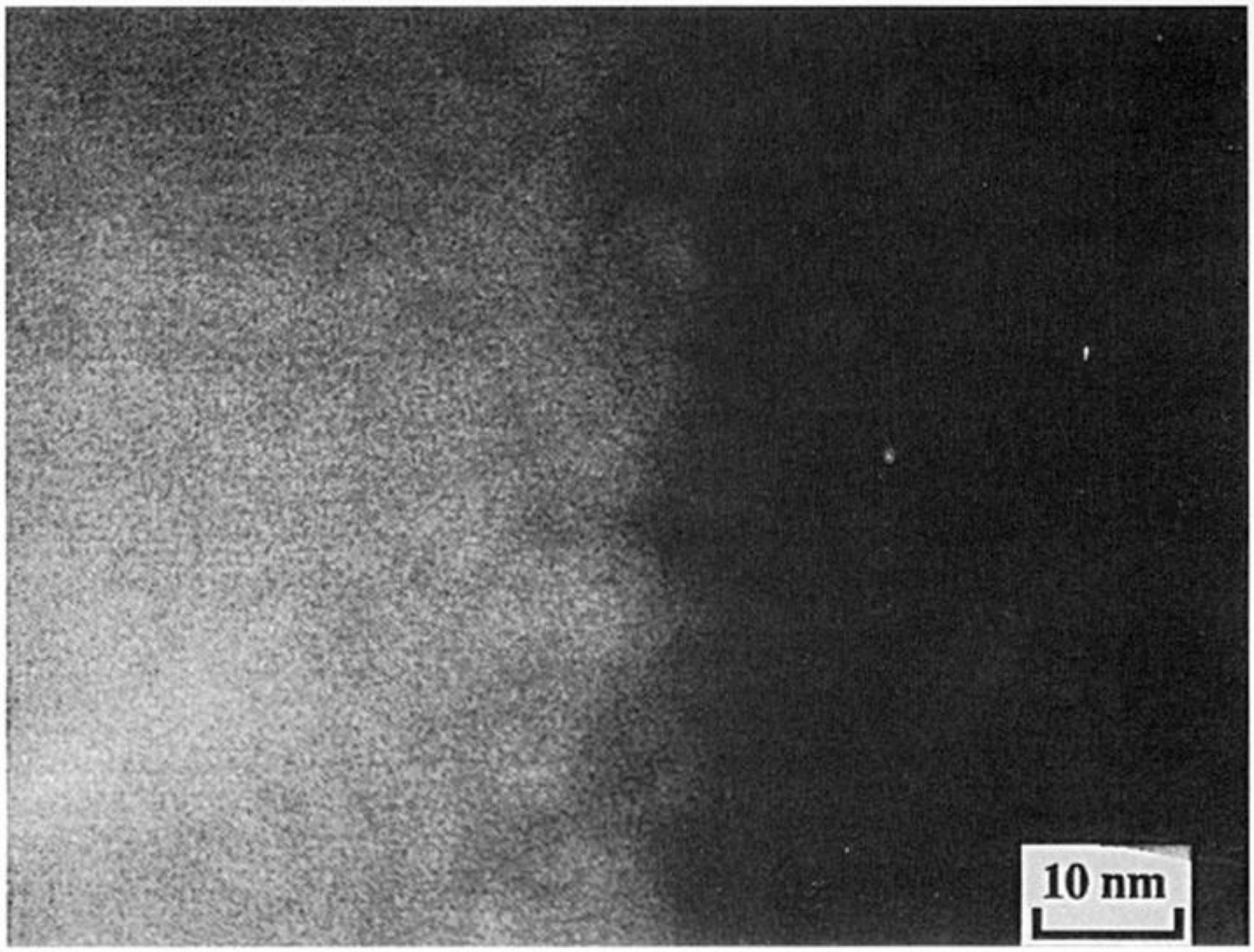

Downloaded from rsta.royalsocietypublishing.org

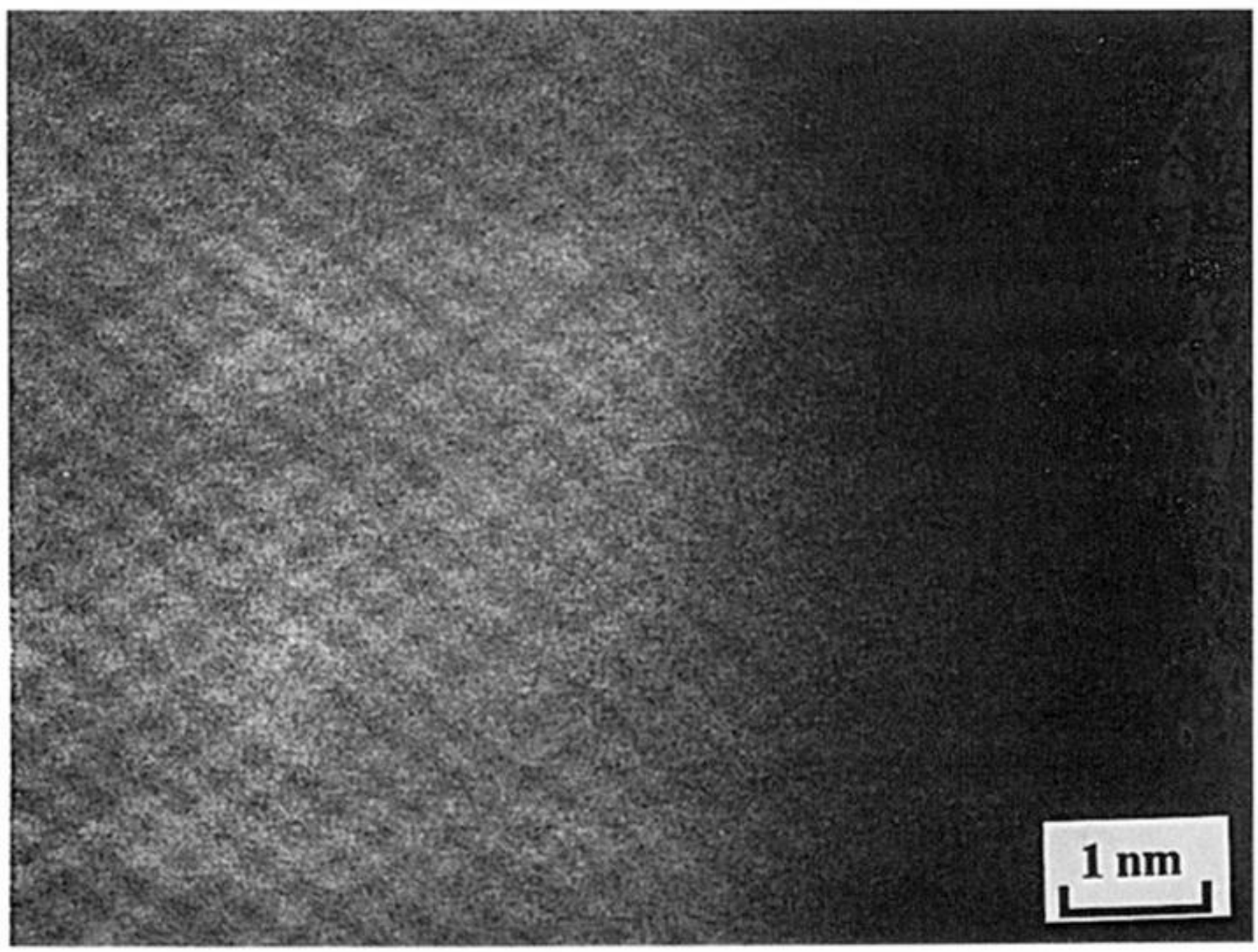

gure 13. Z-contrast image of an amorphous–crystalline interface in ion-implanted Si (100): (a) w magnification view showing 10 nm scale roughness; (b) high magnification image showing dividual dumbbells.

PHILOSOPHICAL TRANSACTIONS OF THE ROYAL SOCIETY A MATHEMATICAL, PHYSICAL & ENGINEERING SCIENCES